Real time hybridization studies by resonant waveguide gratings using nanopattern imaging for Single Nucleotide Polymorphism detection

Kristelle Bougot-Robin, Rimantas Kodzius, Weisheng Yue, Longqing Chen, Shunbo Li, Xi Xiang Zhang, Henri Benisty, Weijia Wen

Real time hybridization studies by resonant waveguide gratings using nanopattern imaging for Single Nucleotide Polymorphism detection

Kristelle Bougot-Robin · Rimantas Kodzius · Weisheng Yue ·
Longqing Chen · Shunbo Li · Xi Xiang Zhang ·
Henri Benisty · Weijia Wen

Abstract 2D imaging of biochips is particularly interesting for multiplex biosensing. Resonant properties allow label-free detection using the change of refractive index at the chip surface. We demonstrate a new principle of Scanning Of Resonance on Chip by Imaging (SORCI) based on spatial profiles of nanopatterns of resonant waveguide gratings (RWGs) and its embodiment in a fluidic chip for real-time biological studies. This scheme allows multiplexing of the resonance itself by providing nanopattern sensing areas in a bioarray format. Through several chip designs we discuss resonance spatial profiles, dispersion and electric field distribution for optimal light-matter interaction with biological species of different sizes. Fluidic integration is carried out with a black anodized aluminum chamber, advantageous in term of mechanical stability, multiple uses of the chip, temperature control and low optical background. Real-time hybridization experiments are illustrated by SNP (Single Nucleotide Polymorphism) detection in gyrase A of *E. coli* K12, observed in evolution studies of resistance to the antibiotic ciprofloxacin. We choose a 100 base pairs (bp) DNA target (~30 kDa) including the codon of interest and demonstrate the high specificity of our technique for probes and targets with close affinity constants. This work validates the safe applicability of our unique combination of RWGs and simple instrumentation for real-time biosensing with sensitivity in buffer solution of ~10 pg/mm^2. Paralleling the success of RWGs sensing for cells sensing, our work opens new avenues for a large number of biological studies.

K. Bougot-Robin (✉)
Institute for Advanced Study, Hong Kong University of Science and Technology, Clear Water Bay, Kowloon, Hong Kong
e-mail: kristelle_robin@yahoo.fr

R. Kodzius · W. Wen
KAUST-HKUST Micro/Nanofluidic Joint Laboratory, The Hong Kong University of Science and Technology, Clear Water Bay, Kowloon, Hong Kong

R. Kodzius
Computer, Electrical and Mathematical Sciences & Engineering (CEMSE), King Abdullah University of Science and Technology, 4700 King Abdullah University of Science and Technology, Thuwal 23955-6900, Kingdom of Saudi Arabia

S. Li · W. Wen (✉)
Department of Physics, Hong Kong University of Science and Technology, Clear Water Bay, Kowloon, Hong Kong
e-mail: phwen@ust.hk

W. Yue · L. Chen · X. X. Zhang
Advanced Nanofabrication, Imaging and Characterization Core Lab, King Abdullah University of Science and Technology, Thuwal 23955-6900, Kingdom of Saudi Arabia

H. Benisty
Laboratoire Charles Fabry, Institut d'Optique Graduate School, 2 Avenue Fresnel, CNRS, Univ P Sud, 91127 Palaiseau, France

1 Introduction

Detection of biological interaction has applications in many fields, such as medical diagnosis, drug discovery, food safety, environment monitoring or bioterrorist threats. Detection methods involve transduction of the interaction into a measurable signal (optical, calorimetric, electrical, electrochemical, magnetic or acoustic signals). Screening a large number of reactions in parallel is essential in most of these domains. For this purpose, biological species ("probes") are commonly

immobilized on a chip surface to capture immersed molecular targets from a biologic sample. Imaging techniques are intrinsically multiplex and hold the leading position for high-throughput screening in microarray format. Fluorescence imaging involves labeled targets which bind to immobilized probes. It was first developed by Affymetrix (Fodor et al. 1993). The sensitivity for visible and near-infrared wavelengths, nowadays, is not much limited by the power of the source or the detector sensitivity, but rather by the extraction and amplification of the signal of interest from the spurious background. While confocal detection is known to provide single molecule detection, it is not much applicable at the scale of microarrays (Martinelli et al. 2007; Bally et al. 2011). Various strategies have been developed to improve the sensitivity of fluorescence imaging. They are based on fluorescence enhancement by reinforcing the interaction of labels with the electric field of the exciting radiation at the chip surface either using plasmonic guided waves (Tawa et al. 2008), multilayer substrates (Choumane et al. 2005) or nanostructured dielectric chips (Ganesh et al. 2007). An important drawback of fluorescence is that it involves the use of labels which can sterically hinder the biological interaction of interest. In addition to extra costs and time induced by labeling, fluorophores also suffer from photobleaching which can distort or bias the analysis and/or require instrumentation control to reduce the exposure time (Xiang et al. 2007). Some other widely used optical methods detecting biomolecular events at a chip surface exploit the induced change of refractive index through detection in resonant conditions. The most developed technique for this purpose is surface plasmon resonance imaging (SPRi) (Jordan et al. 1997). In SPRi, the control of metallic surface quality and uniformity can be an issue as it widely impacts the local amount of spurious non-specific interactions (Nogues et al. 2012). It should also be kept in mind that the confinement of the mode and the shape of the resonant response mainly depend on the nature of the plasmon (transporting metallic layer). Higher sensitivities in imaging would demand sharper resonant curves and higher quality factors, which are however intrinsically limited in SPR due to losses in metal, traditionally gold (Au). Silver (Ag) or aluminum (Al) could bring higher sensitivities; however, for biocompatibility, Au remains by far the preferred choice. Through structuration of the chip surface, localized plasmons allow some sharpening of the resonance shape and bring new configurations for biosensing (Dhawan et al. 2011). Nanoparticles based array readers involving localized plasmon were also demonstrated successfully for biology applications (Olkhov et al. 2010, 2012).

The dielectric resonant waveguide grating (RWG) approach can thus be expected to overcome some of the plasmon limitations (Yeatman 1996). However, direct RWGs 2D imaging, this competing direct label-free multiplex method, has not been extensively addressed for biological detection in liquid samples. At the heart of the system, the resonant grating approach resembles the surface plasmon resonance approach: the guided wave is localized close to the surface in the high index layer of the chip (at least the main spatial harmonic) and interacts with the biological layers immobilized on its surface. Biological detection using resonant grating has been demonstrated and commercialized using the shift of the resonance position peak either with spectro-imaging detector (Li et al. 2004) or with a tunable light source to scan the wavelength (Ferrie et al. 2010). Angular-scan is an alternative but requires highly sensitive mechanical control (George et al. 2010) and has thus enjoyed much less development. These are indirect ways of obtaining images of RWGs chips using multispectral/multiangular instrumentation.

Fully multiplexed imaging of grating consists in illuminating the chip near resonance by filtering the incident light spectrally and angularly, and imaging either the change of reflected signal intensity, or of a spatial profile on the chip. RWGs imaging uses the same principles as SPR imaging, but allows through the grating parameters, far more flexibility in term of resonance shape, central wavelength, coverage with biomolecules/cells, and optical configuration. Previous work demonstrated that direct 2D imaging of a full surface grating allows detection of biomolecules for end-point detection of a monolayer of biomolecules (Bougot-Robin et al. 2010), indeed in the UV photon range. Experimental detection of biological interaction in real-time (fraction of monolayer prior to stabilization) and in aqueous medium requires to detect weaker variations of the reflectivity, typically reduced by a factor of 3 to 6. Real-time experiments are more prone to background variations, for instance from biological or optical origins. Therefore, we recently proposed a scheme to take benefit of both simplicity of direct imaging and robustness allowed by using a scan or an intensity sequence (Bougot-Robin et al. 2012a).

The general idea relies on having a resonance-scan profile dimension integrated in the chip itself, instead of *ex-situ* scanning through instrumentation (some form of scanning detector), and on further exploiting these spatial resonant profiles through simple monochromatic imaging. We name this rather general principle "SORCI": Scanning Of Resonance on Chip by Imaging. Considering that the whole measurement involves multiple spots *and* a scan of a resonance to determine its local shift, the concept of multiplexing can be generalized to scanning as well. Through a "nanopattern" scanning chip and imaging, the SORCI approach addresses the case of multiplexing of the resonance itself (for a given biology) at distributed places onto a chip. The use of such a "nanopattern scanning" at various places of the chip allows tracking of a resonance among these places, with a given biological assay, and thanks to 2D direct imaging, a biologically-multiplexed version of SORCI is intrinsically performed in parallel.

In the present work, we implement on-chip microfluidic integration with "nanopattern" scanning chips to demonstrate the application of our technique to *in situ* real-time hybridization measurements. We also introduce the chip functionalization process of individual areas and the hybridization sequence. We choose to study SNP detection using a 100 bp DNA fragment, corresponding to a molecular weight of ~30 kDa, a typical size of Polymerase Chain Reaction (PCR) product or of proteins. Such a choice, demanding both in term of sensitivity and specificity, validates the potential of our technique for a large number of applications (Kwok et al. 2003). Using temperature control of our hybridization chamber, this work validates the wide potential of our spatial 'Peak-tracking' principle combined as a chip-based technique for real-time and label-free operation, crucial for bio-detection.

2 Nanopattern scanning chips

2.1 Single grating resonant response (≡ spectral resonant response of one micropad)

A resonant waveguide grating consists of a waveguide with a grating whose periodicity allows the coupling of an impinging plane wave by satisfying a phase-matching condition. In Fig. 1a, we give the general idea of a RWG structure and its resonant response depending on the wavelength as most classically measured. The shift of the resonance reveals the amount of hybridized biomolecules, with the reference (Ref) being the situation without hybridized molecules, only probes and buffer. As schematized in the inset, the waveguide structure consists of a high-index layer in which the wave is guided, supported by a low index layer which serves as a support or as a spacer to reduce losses in case of configuration on a metal substrate (Bougot-Robin et al. 2010). The waveguide is textured with a resonant waveguide grating to fulfill phase matching and couple the incident wave to the surface wave, this latter physically acting as an energy reservoir (Tonchev and Parriaux 2012). The structure is optimized for the detection of green radiation ($\lambda = 545$ nm) near normal incidence ($\theta = 18°$). We choose TM polarization, which is more dispersive and has in the meantime a narrower resonance profile. The waveguide is based on a silicon nitride layer of index $n \approx 2.1 + 0.0026i$ that covers the glass substrate of index $n \approx 1.47$. The chip is designed for backside imaging so the incident beam direction is unaffected by the analyte solution refractive index. A reasonably optimized chip for our (λ, θ)=(545 nm, 18°) illumination condition consists of a single grating structure of period $\Lambda = 450$ nm with filling factor $f = 0.5$, and a guiding layer of thickness 0.27Λ and etched on a thickness of 0.11Λ. The biological layer is located on the top of the weakly corrugated high-index layer in order to strongly interact with the guided wave. This extra layer induces a change of the local index in the vicinity of the chip surface sensed by the guided optical mode's evanescent tail, and in turn, through a change of the mode's effective index, a change in resonance conditions. In line with our experiments, the considered ambient medium has a refractive index of $n \approx 1.3595$, corresponding to our selected buffer refractive index. The biological layer is modeled as a thin layer of index 1.45 and thickness 2.2 nm. The structure reflectivity is calculated using a scattering matrix formalism (Li 1996; David 2006).

In the conventional scheme of scanning resonance through *ex situ* instrumentation, a single grating is used and the bioarray spectral-images are acquired, involving either a fast-tunable light source and a 2D detector or a spectro-imager with a continuous source, as illustrated on Fig. 1b. These configurations are demanding in term of cost of the instrumentation, as well as amount of data for real-time imaging.
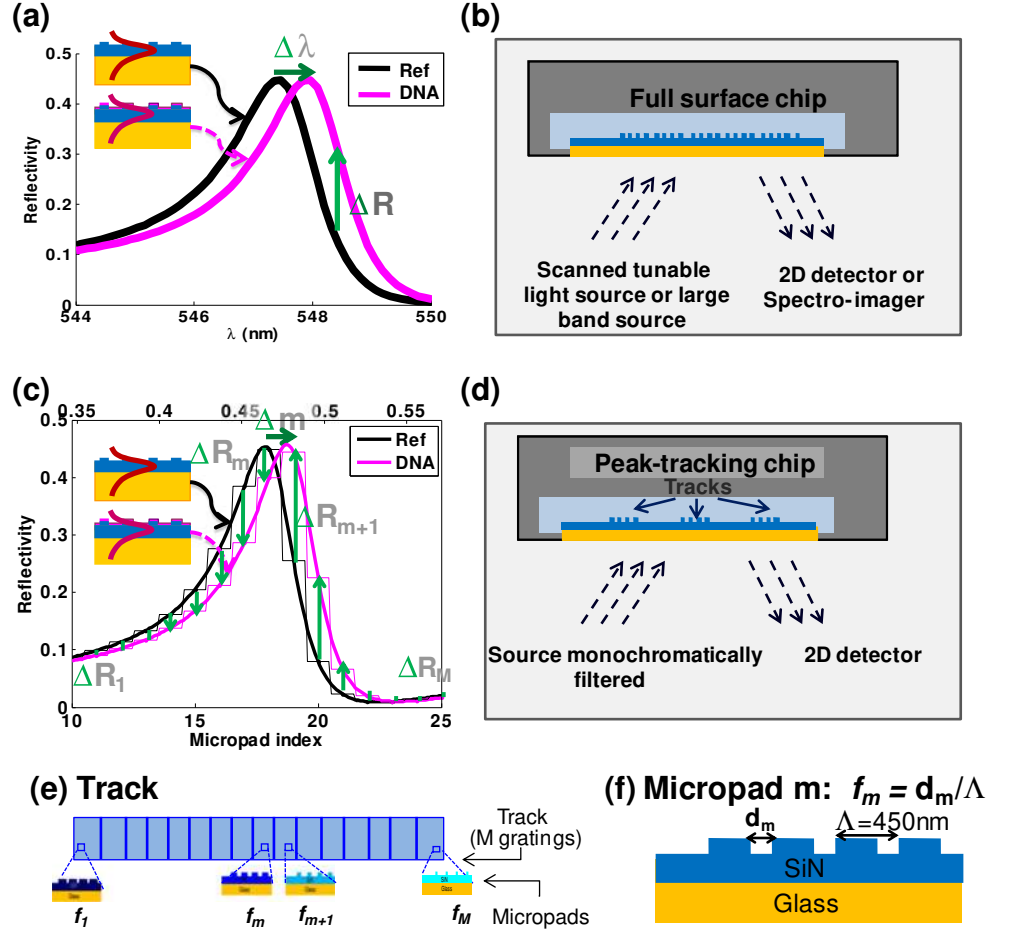
2.2 "Nanopattern" profiles robustness through direct 2D imaging

Our proposed alternative to these instrumental scans is to slowly vary a parameter of the nanopattern and scan *in situ* the spatial information measured by simply exploiting a monochromatic direct imaging configuration (Bougot-Robin et al. 2012a). Thus, in (λ_0,θ_0) illumination conditions, we can get a near-resonance intensity scan (equivalent to getting the sequence difference ΔR_m from the two curves of Fig. 1a) from a simple picture. Given the fabrication limitations and in view of an overall N×P tracks placed in a 2D microarray disposition, we choose to vary the pattern top geometry and realize M discrete grating units ("micropads") of different groove width d_m and thus variable air filling factor f_m where $m = 1...M$ stands for the micropad index. From our electron beam lithography limitation, the groove width can be varied by step $\Delta d = 4$ nm, which corresponds to a filling factor variation by steps of $\Delta f = \Delta d / \Lambda = 0.089$. The corresponding profile is given in Fig. 1c, where the step-wise shape of the curve reflects the discrete f_m, each of the step providing its own ΔR_m value with $m = 10$ to 25 shown here. The resonance appears thus as shifted by a certain number Δm of micropads units, which might be a fractional value subsequent from profile analysis. The scheme of the direct imaging measurement set-up is given in Fig. 1d. In Fig. 1e, we illustrate the sequence of M micropad units, grouped in "tracks" for SORCI multiplex detection, with more details on the m-th micropad unit ($f \equiv f_m$) in Fig. 1f.

2.3 Shape of the resonance and sensitivity

Effective waveguide refractive index and mode profile depend on the structure geometry and indices. The latter can be tuned according to the size of biological elements to detect, to

3

Fig. 1 a Typical shape of a resonant grating reflectivity spectrum, without (*black line*, Ref) and with (*pink line*, DNA) biological layer. Biological layer induces a shift $\Delta\lambda$ of the reflectivity curve **b** Scheme of the optical set-up to measure spectral information in 2D: either a tunable light source with a normal camera, or a broad band source with spectro-imager detector are used **c** Implementation of SORCI: a nanopattern made of $m=1\ldots M$ grating micropads with varying geometry is used to scan around the resonance. Here $m=10$ to 25 covers the peak **d** Direct imaging set-up with our specially designed "Peak-tracking chip" **e** Detail of a track of M micropads with variable filling factor **f** Grating in a micropad with period $\Lambda=450$ nm and groove width d_m. The air filling factor f_m varies from $f_1=0.44$ to $f_M=0.57$ in (**e**)

maximize light-matter interaction in the biomolecules region and obtain an optimum "signal to background ratio". A proper mode confinement grants a large sensitivity to surface modification, in proportion of the fractional overlap Γ of the mode tail with the biologically modulated region. Thus, depending on molecules sizes, the chosen characteristics of the RWG structure (materials, thickness of the layers, etching depth h, filling factor f, period Λ) will result in a mode offering an optimal overlap Γ with the molecular layer, thus increasing signal to background information (Kunz et al. 2006).

Generically, it is a compromise between strong confinement, which means field concentration in a thin slice in general, and the relative amplitude at the interface, which decays when the mode profile is too confined. Such an optimally confined mode has to be exploited further through a preferred grating coupling in order to produce a high sensitivity to an induced change of refractive index at the chip surface.

It is well known by practitioners that both issues, confinement and coupling, interact, so that varying the grating depth parameter already yields rich data. We thus illustrate the trends appearing when tuning mode confinement through etching depth, notably on the resulting shape of the resonance spatial profile. The "Peak-tracking chip" design is as described in the

previous section, having several tracks on SiN/glass substrate, with tracks composed of micropad units of constant period $\Lambda=450$ nm, with varying filling factor f_m between $f_1=0.35$ and $f_{33}=0.65$ by step $\Delta f=0.0089$. Etch methods are such that all micropads have identical etching depth (no "lag" for narrow grooves), and only the filling factor changes among micropad units of a given track.

The guided mode effective index $n_{eff}(\lambda)$ depends on the RWGs parameters. The wavevector of the guided mode of interest in our chip can be written as:

$$k_{//}^{biochip} = n_{eff} \times (2\pi/\lambda)$$

where n_{eff} is the mode effective refractive index associated to a given (λ_0, θ_0) illumination condition, and for a grating of given geometrical parameters.

In Fig. 2 we give the spatial profiles over the tracks as well as the electric field distribution at a wavelength $\lambda_0=550$ nm and in TM polarization. Figure 2a, b, c correspond to various etching depth, respectively $h=0.06\Lambda$, $h=0.11\Lambda$, and $h=0.25\Lambda$. The incident angle chosen in the simulation is
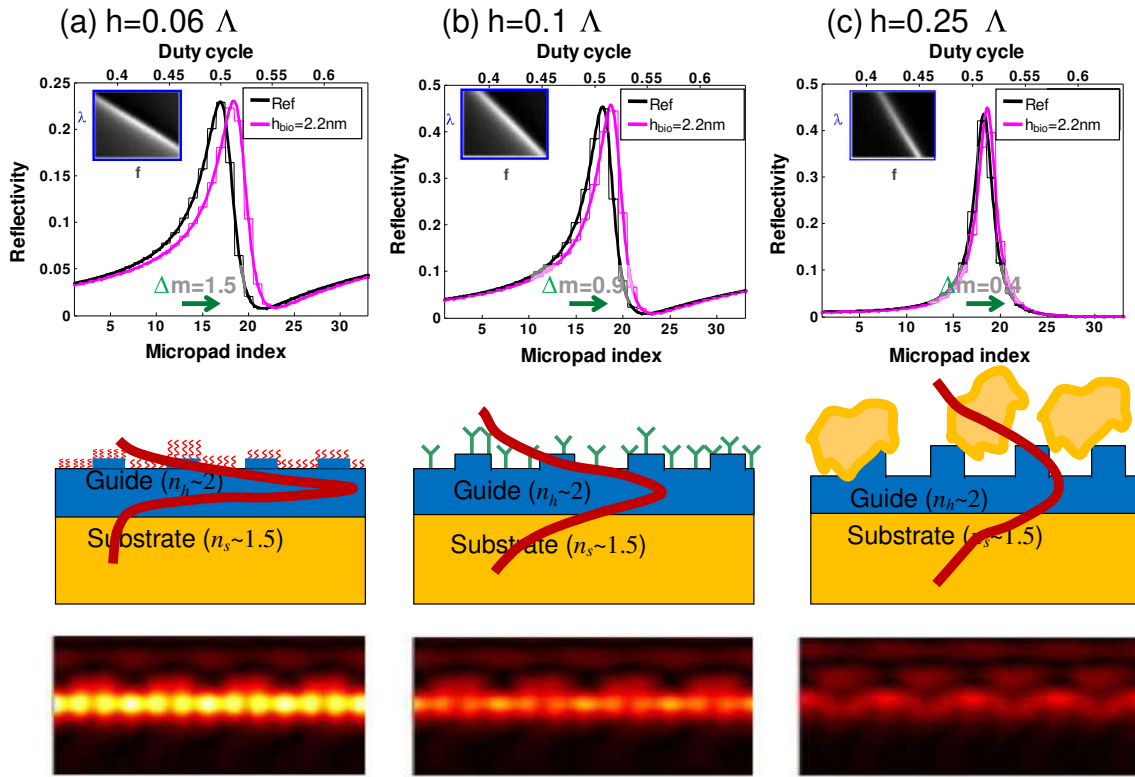
Fig. 2 Reflectivity spatial simulated profiles around the resonance with and without biological layer of thickness 2.2 nm and index 1.45 **a** For an etching depth of 0.06Λ, corresponding to a quality factor $Q\sim420$ and a dispersion of 326 micropad/RIU **b** For an etching depth of 0.11Λ, corresponding to a quality factor $Q\sim157$ and a dispersion of 224 micropad/RIU **c** For an etching depth of 0.25Λ, corresponding to a quality factor $Q\sim35$ and a dispersion of 146 micropad/RIU. Below each graph is shown a scheme and the simulated map of the electric field confined in the high index layer. The insets next to profiles are the (λ,f) intensity maps. They show how the width of spatial profiles at fixed $\lambda=\lambda_0$ depends on the filling factor

slightly adjusted (from 16° to 22°) so as to match the coupling condition at a wavelength $\lambda_0=550$ nm.

From the spatial profiles displayed in Fig. 2, it can be seen that the spatial resonance profile covers less micropads when the etching is deeper. A thicker "etched layer" means that for a given filling factor, the change of effective index of the waveguide will be larger, and consequently, over the whole filling factor range, the span of effective index of the waveguide will be large. Therefore, less micropads structures satisfy the phase matching conditions, and the profile has a smaller width in micropad units.

Simultaneously, as the etching depth is increased, for a given filling factor f, it first tends to bury the guided mode further away from the waveguide surface, but this trend eventually reverts. Indeed, as it can be guessed, by homogenizing the etched layer as an average index, a deeper etch of a given waveguide leaving a very thin core induces a decrease of the mode effective index and a deconfinement of the mode itself. Such a mode corresponds to a longer tail and thus a better overlap with larger cells, and may for instance be chosen for the sensing of cells, with a size on the order of 1 μm, as illustrated in (C).

We also studied the dispersion (vs. RIU) of our structures. For this determination, we consider a constant refractive index at the chip surface. For etch depth of $h=0.25Λ$, $h=0.11Λ$ and $h=0.06Λ$, the dispersions (resonance shift) are respectively of $\Delta m=146$ micropad unit/RIU, $\Delta m=224$ micropad/RIU and $\Delta m=326$ micropad/RIU.

The quality factor of the resonance is a representative parameter of both the dispersion and shift expected for a refractive index change. It is defined by $Q=\lambda/\Delta\lambda_{1/2}$, where $\Delta\lambda_{1/2}$ is the resonance full-width at half maximum (FWHM). From spectroscopic simulation, considering a constant filling factor $f=0.5$, an etch depth 0.06Λ corresponds to a quality factor $Q=\lambda/\Delta\lambda_{1/2}\sim420$, decreasing to $Q=160$ for an etch depth of 0.11Λ, and collapsing to $Q=35$ for an etch depth of 0.25Λ.

As a comparison, the surface plasmon resonance exhibits a quality factor of the order of 10 without structuration, which can be increased to a still quite modest $Q\sim20$ with metallic grating structuration (Dhawan et al. 2011; Hu et al. 2010). Therefore, the resonant dielectric grating approach can lead to a much better sensitivity than the classical Surface Plasmon Resonance imaging method, e.g. with $Q>100$ values that are still not too demanding in terms of operating signal and signal-to-noise ratio.

2.4 Horizontal propagation of the mode

As our detection method is imaging, we also study the horizontal propagation of the RWG's underlying mode. The spatial in-plane extent of the guided mode Δx is defined by the distance at which its amplitude is divided by 2. It is related to the spectral finesse F of the resonance by the group velocity v_g according to $\Delta x = \ln(2)$ F λ / n_g (Yeatman 1996), where n_g denotes the group index according to $v_g = c/n_g$. To retain the imaging properties that are much desired for assessing a proper operation, considering a biological spot size of 200 μm, a spatial extent of $\Delta x \sim 20$ μm or less is adequate. For a wavelength $\lambda \sim 550$ nm and a group index $n_g \sim 2$, it corresponds to a finesse $F \sim 200$, meaning that resonances with quality factor $Q \leq 200$ are in principle acceptable. For micropads disposition, we choose a vertical alignment (grating grooves parallel to track long dimension) to avoid propagation between neighboring micropads.

3 Materials and methods

3.1 Profile position determination using correlation analysis

Since our resonance profiles have Fano lineshapes, usual analytic fitting such as Lorentz or Gauss do not always give an accurate determination of the resonant position due to asymmetry and tail contribution. Therefore, we use a correlation approach to determine the resonance peak shift, which allows robust and accurate fitting of peak position taking into account the asymmetric shape of Fano resonance and many fequatiodistortions and noise contribution (Bougot-Robin 2012b). The general idea is to calculate the correlation between the signal image $\overline{S}(t)$ at a time t with the reference image $\overline{S}_{ref}$ to determine the instantaneous peak shift and deduce the amount of bounded molecules. This method could be used in other flavors of the general SORCI principle.

Images are 2D matrix, of dimensions $D_x \times M\ D_y$, where $M = 33$ is the number of micropads, and D_x and D_y are the number of pixels spanning a micropad in both directions. $\overline{S}_{ref}(i,j)$ and $\overline{S}(i,j)$ are the reference and signal at a time t at (i,j) position of the 2D matrices. Except spurious contributions such as noise or other distortion effects, the D_x lines ideally have the same signal. We therefore calculate the correlation on each of the lines between the signal and the reference images and average over the different lines. The correlation function is given by Eq. (1):

$$C(\Delta j) = D_x^{-1} \sum_j \sum_i \overline{S}(i,j) \otimes \overline{S}_{ref}(i,j) \qquad (1)$$

To increase the accuracy of this correlation beyond the micropad unit (the step in question) and determine precisely the position of the resonance, we calculate the centroid of the correlation function after correcting it from its average and bringing it at a high power exponent (Bougot-Robin et al. 2012b). The corrected correlation function C' is thus given by Eq. (2), and we use here an exponent $k = 10$.

$$C'^k = \left(C - <C^2> \right)^k \qquad (2)$$

It results in a non-integer spatial shift determination Δm_{sensed} of the track profile may be quantified in micropad unit as given by Eq. (3).

$$\Delta m_{sensed} = \sum \Delta m\, C'^k(\Delta m) / \sum C'^k(\Delta m) \qquad (3)$$

This "improved centroid algorithm method" allows to eliminate a large part of the biases due to "windowing" effects or to the presence of a substantial background in the tails (Baik et al. 2007; Li et al. 2008).

The shift is considered as proportional to the biomolecules layer thickness variation for substantial concentration ranges.

3.2 Chip fabrication and characterization

In this paper, in spite of the more general potential, we focus on the detection of small molecules (~1 to 5 nm size), which are thus localized close to the chip surface.

Our structure consists of high-quality borosilicate glass substrate (roughness <0.5 nm) of 500 ± 10 μm thickness from Plan Optic, with optical index $n = 1.47$. It is first covered by PECVD (Plasma Enhanced Chemical Vapor Deposition) silicon nitride layer of thickness ~150 nm and index $n = 2.1 + 0.0026i$ (determined by ellipsometric measurement on a SiN/Si substrate comparative structure).

The nanopattern is realized by electron beam lithography (e-beam). To circumvent charging effects, the chip is first covered by a 5 nm Cr layer deposited by sputtering. It is then spin-coated by ZEP-7000 photoresist, hard-baked, further exposed by e-beam and followed by photoresist development. The chromium layer is etched through by a RIE (Reactive Ion etching) process, and we then strip the photoresist using O_2 plasma, and etch the silicon nitride layer by another RIE. Finally, the chromium layer is removed using a chromium etchant solution.

The etching depth is determined through AFM characterization to be of $\sim 51.7 \pm 0.3$ nm, or equivalently 0.11Λ. As illustrated in the previous section Fig. 2b, this corresponds to a quality factor $Q = 160$ with a dispersion of 224 micropad/RIU. In Fig. 3, we give AFM pictures of several micropads with various filling factors. Etching depth is confirmed to have a good homogeneity on the whole track. Although the filling factor cannot be determined precisely through AFM as the tip cannot follow the vertical slope of the gratings, the filling
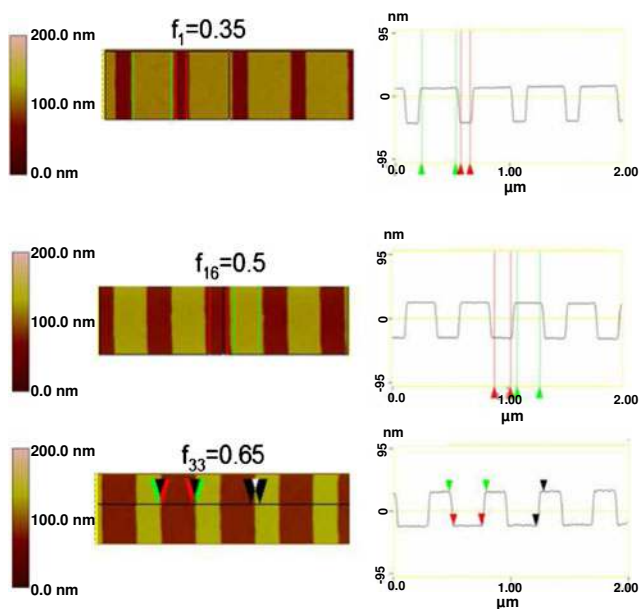
Fig. 3 AFM images for various filling factors (f_1=0.35, f_{16}=0.5, f_{33}=0.65) as well as corresponding profiles. The etching depth is of h=51.7±0.3 nm and is homogeneous on the whole track, independently of the filling factor

factor of the fabricated structures is close from the targeted values, varying from f_1=0.35 top f_{33}=0.65.

3.3 Localized gratings versus spot functionalization

Another advantage of localized gratings over flat surface is to somehow substitute to the classical spots obtained by droplet-based techniques. Droplet homogeneity requires some know-how due to evaporation and deposition. Here, we propose to immobilize the probes on the whole tracks with overnight incubation in humidified environment. The number of pixels/spots can be increased by using a square/rectangular shape. To control functionalization on localized tracks areas, we design PDMS fluidic chambers. Our structure with three adequate chambers of 1.5 mm×4 mm poses no design problem and is classically fabricated by soft lithography. In addition to fit to the tracks areas, such chambers allow to avoid inhomogeneous evaporation, which is often an issue when using droplets. Taking into account covered area as well as the horizontal spatial extent of the mode, we eventually chose rectangular grating shapes of 100×200 µm^2. With a 10 µm horizontal extent, 2.5 % of spot pixels at the edges may carry mixed information and have to be discarded upon image analysis. Localized gratings can also be used to increase spot densities. In that case, deeper etching outside of the "spot array" sensing zone would be necessary to stop the guided mode propagation, thus suppressing cross-talk between various biological zones with only minor technological difficulties (Abbas et al. 2011; Chang et al. 2011).

The dimension of micropads of 100×200 µm^2 leaves room for detection of a few tens or even hundreds of reactions in parallel. As a first demonstration, we will focus on 3 tracks, two with the probes of interest (mutated and wild type) and one for negative control.

3.4 Biochemical preparation

3.4.1 Probe immobilization process

In Fig. 4, we give a scheme of the successive steps of the probe immobilization process. The oxygen density of the silicon nitride layer $Si_xN_yO_z$ is higher than the maximum possible density of DNA probes occupancy (considering a maximum density of 10^{13} probes/cm^2 = 0.1 probe/nm^2), so we can choose a classical hydroxyl-based immobilization chemistry. The chip surface is first activated using O_2 plasma and 0.1 M NaOH bath, and further silanized using an aminosilane molecule on its whole surface by putting it for 2 h in a 1 % concentrated silane solution, using an (3-Aminopropyl)triethoxysilane (APTES) in ethanol/water 95:5 solution. The details of activation, chip cleaning, silanization, cleaning of unbounded molecules and baking are given in Fig.4a.

To immobilize various probes on the various tracks, we fabricated a PDMS cover structure with separate chambers. Our multiplexing scheme consists in coating different probes in distinct chambers of the chip. The top and side views of these PDMS chambers on our chip are illustrated in Fig. 4b.

For the grafting of probes on the silanized chip surface, as illustrated in Fig. 4c, we introduce 5 µM DNA solution re-suspended in 3X SSC solution (Saline-Sodium Citrate, which serves to control stringency) 1.5 M betaine and incubate it in the chambers overnight, in a humidified environment. The PDMS chambers are then removed and the chip is successively cleaned in solutions of various compositions of SSC and SDS (sodium dodecyl sulfate, which acts as an ionic surfactant). Successive solutions compositions are: (1X SSC, 0.2%mSDS), (0.1X SSC, 0.2%m SDS), and (0.1X SSC).

3.4.2 "Peak-tracking Chip" and fluidic chip passivation

The chip is then placed on our fluidic structure described in more details in the next subsection. Prior to hybridization experiments, the chip and fluidic structure are passivated by introducing a blocking buffer consisting of 4X SSC, 0.1%m SDS, 0.1%m BSA (bovine serum albumin), and 4%v isopropanol. It is then successively cleaned by introducing the following solutions for 2 min: (1X SSC, 0.2%m SDS), (0.1X SSC, 0.2%m SDS), and (0.1X SSC). Finally, the fluidic chamber chip is filled with a specific hybridization solution (5X SSC, 0.1%m SDS, 25 % formamide) without DNA, and
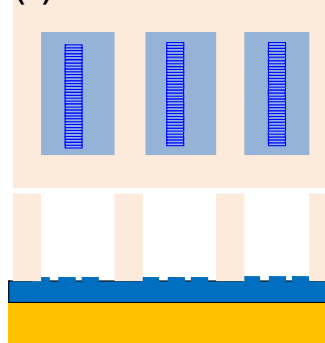
Fig. 4 a Chip activation, cleaning and silanization with APTES silane **b** PDMS mold with separate chambers is placed on the silanized chip to have each track in a separate chamber and put each probe on its track **c** Overnight incubation of probes in 3X SSC (Saline-Sodium Citrate), 1.5 M betaine at 5 μM concentration **d** Remove PDMS structure and clean the chip to remove unbounded probes present on the surface; measure fluorescence for control

(a) Cleaning and silanization

Hydroxy based silanization process using APTES (amino-propyl-tri-ethoxy-silane)
- Surface activation (O2 plasma and 0.1M NaOH)
- Successive cleaning in ethanol/water solutions
- Incubation with APTES
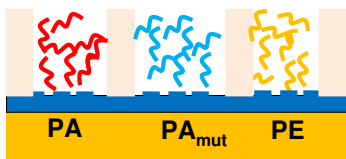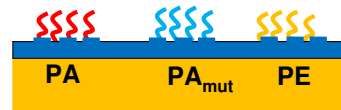- Successive cleaning in ethanol/water solutions
- Baking

(b) PDMS chambers

(c) Probe incubation overnight
40 μL probe at concentration 5 μM in 3X SSC, 1.5 M betaine is introduced in each chamber

PA   PA$_{mut}$ PE

(d) Cleaning
2 minutes successive cleaning in the solution (a) 1X SSC, 0.2% SDS, (b) 0.1X SSC, 0.2% SDS, and finally (c) 0.1X SSC.

PA   PA$_{mut}$ PE

placed on the set-up prior to probes introduction to adjust the experimental configuration.

3.5 Fluidic chip and optical set-up

To prevent background signal, the optical chamber is fabricated in aluminum and further black anodized by an outsourced company. Anodizing is a process to electrolytically coat a metallic surface with a protective oxide. The fluidic chamber is immersed in successive bath for cleaning and anodized in a bath with water and acid used as the electrolyte. A cathode is mounted to the inside of the anodizing tank and the aluminum acts as an anode, so that oxygen ions are released from the electrolyte to combine with the aluminum atoms at the surface of the part being anodized. The acid action is balanced by the oxidation rate to form a coating with nanopores which can accept dyes easily. The dye-staining process is followed by sealing to close the pores, to retain the dyes, as well as to increase corrosion resistance and absorption of unwanted elements. With black background, reflectivity of the incident beam which travels through the biological sample is low, and we can get rid of interference background resulting from thickness variation of the order of the wavelength (due to various instabilities such as moving fluids). This choice is also guided by stabilization requirements for our optical experiments. The optical window is the chip substrate itself, with its sensing waveguide on the biological solution side. The fluidic impermeability is ensured through O-ring sealing. This configuration is highly advantageous in term of possibility to reuse the chip (which may be cleaned by O$_2$ plasma to reuse it a few times) in comparison for instance to a

configuration with carbon-PDMS and plasma bonding. It also allows good mechanical stability (chip is maintained in sandwich between back and front side cover, using screws to obtain mechanical pressure for proper sealing). In Fig. 5a, we give a scheme of the chip mounted on its holder.

Another advantage of a black-anodized aluminum chamber is the easy implementation of temperature control. To regulate hybridization temperature, five 5 Ω resistors rated for 30 W with holes through for fixation are hold with screws in contact to the holder. A thermocouple is fixed in the aluminum chamber so the temperature can be controlled and regulated using a thermocontroller. Pictures of our black anodized aluminum chamber with its resistor heaters are given in Fig. 5b, from backside and front side.

Although rather simple, we believe our fluidic arrangement may benefit to other fluidic experiments, and specifically in the field of imaging, where background and mechanical stabilization are of foremost importance. Its modular aspect is also of interest for the reuse of the chip, and its black background allows on-chip thermal integration without former shading issues (Skafte-Pedersen et al. 2012). The possibility of thermocontrol on the holder itself is also advantageous in term of set-up compactness and cost in comparison to microscope thermocontrolled stages.

Control of temperature is important from a biological point of view, as hybridizations kinetics are temperature-dependent. Moreover, for SNP detection, probes and target have close affinity constants. Through the control of hybridization temperature, the association of a perfect-match probe and its target can be favored against mismatch one. Temperature control is also necessary to avoid refractive indices variation (buffer,
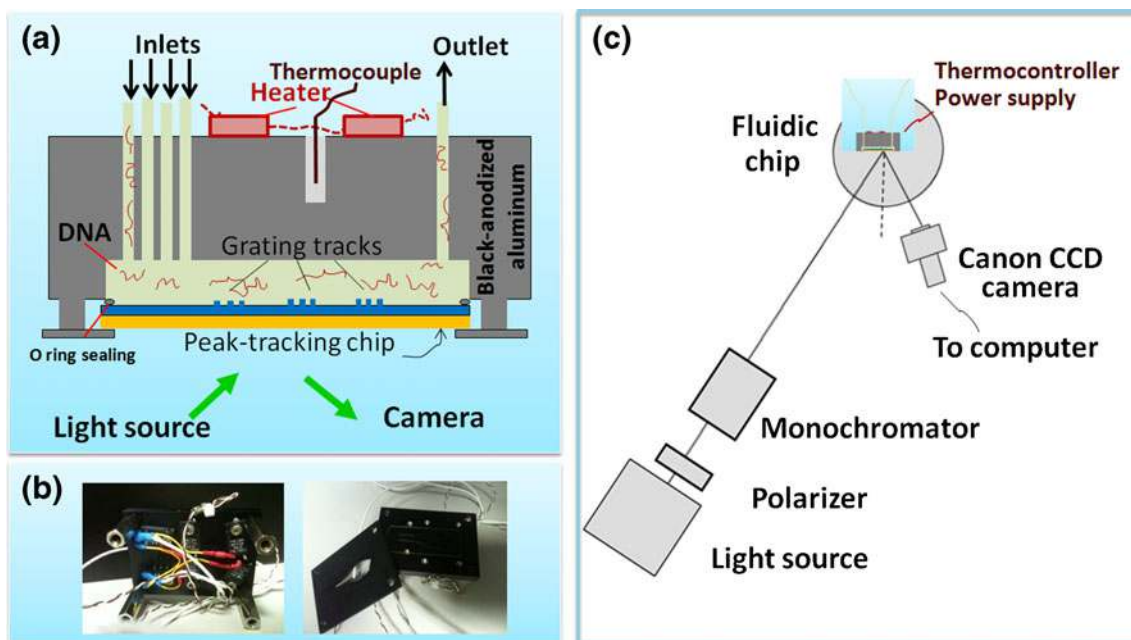
Fig. 5 a Scheme of the chip and of the microfluidic chamber for biological interaction **b** Picture of the fluidic holders, from back side and front side, with 6 resistance heaters and inlets/outlets on backside **c** Optical set-up used to image the chip

chip materials) as these latest are temperature-dependent, and may bias experimental interpretation of resonance shift.

Experiments are based on a reflection set-up composed of a high-power LED from Thorlab Inc., filtered by a monochromator from Zolix, of 30 cm focal length. The incident light is polarized to get TM polarization, and illuminates the sample from its backside. Images are acquired with a Canon EOS 5D camera. In Fig. 5c, we display a scheme of the optical set-up.

In this first work, we choose a configuration taking benefits of widely available optical instrumentation to image our nanopatterned chip. For larger development, some contact imaging configuration may also been studied (Martinelli et al. 2007; Wu et al. 2012), bringing however new issues about the integration of the CCD in close proximity of the chip.

3.6 Gyrase A mutation detection

Increasing resistance to antibiotics is an important issue for health. Understanding complex mechanisms of resistance occurrence and spread through a population is essential.

Studies exploiting micro-structured landscape with micro-habitats of various conditions recently demonstrated that it is possible to induce and accelerate resistance spread in *E. coli* cells. Bacteria were introduced in microfluidic environment with high antibiotic gradients and places of low and high antibiotic concentration. Microfluidic experiments have been further validated by sequencing the genome of resistant colonies selected by replica plating at end-point of the experiment (Zhang et al. 2011a). Antibiotic used as a model was ciprofloxacin, which binds on the DNA gyrase, thus preventing

replication. Resistance to ciprofloxacin could be fixed within 10 h. Whole genome sequencing of colonies from various experiments showed reproducible mutations in 3 genes: a highly-functional missense mutation in the gyrase A gene, at amino acid 87, from Aspartic acid to Glycine, preventing binding of ciprofloxacin on DNA gyrase, as well as mutations in rbsA gene and in the gene coding for marR. While the mutation in gyrase A gene was expected, mutations in the other 2 genes had not been reported previously in the case of ciprofloxacin resistance. Then, although such a pioneering study provides important insights in the emergence and spread of resistance, there is still a lack of information on the temporal and spatial dependence of mutations occurrence, as well as time dependence of the spread of mutation within the population.

Whole genome sequencing techniques are far too expensive to get statistical data and analyze mutations in a whole population. Therefore, such analysis can only be inferred by statistical observables, such as the level of expression of a probed sequence inside the population. Quantifying the proportion of the population that has a given mutation using simpler biosensing techniques, we may therefore analyze much more directly the proportion of the population of a given mutation at a given time t.

We also observed that the evolution of resistance is further accelerated if bacteria have already acquired the phenotype of growth advantage at the stationary phase (GASP) (Zhang et al. 2011b). Further genotypic characterization with GASP bacteria and comparison with wild-type may bring new insight for the understanding of underlying mechanisms.

In this paper, we concentrate our efforts on demonstrating that we can detect selectively the missense mutation observed in gyrase A. We thus design probes to target the mutation at amino acid 87 from Aspartic Acid to Glycine. The designed probes also include a 10-thymine-long spacer for better steric accessibility to DNA probes grafted to the chip. Probes and other DNA sequences including oligonucleotides were synthesized and provided by Invitrogen and have the following sequences:

– Probe PAmut
 5′TTTTTTTTTTTCGCCAGATA**CCG**TGCTAG 3′
 corresponding to the complementary sequence of gyrase A fragment from *E. coli* K12 genome, including codon 87 in its mutated version (mismatch case)
– Probe PA
 5′TTTTTTTTTTTCGCCAGATA**CTG**TGCTAG 3′
 corresponding to the complementary sequence of gyrase A fragment, including codon 87 in its wild version (match case)
– Probe PE
 5′TTTTTTTTTTTTACCGAGCTGTTCCTTGTG 3′
 corresponding to negative control, specific to another unrelated gene from *E. coli* K12 genome.

In order to test our technique, we choose a target consisting of a fragment of gyrase A sequence, including the codon of amino acid 87 in its wild version. It consists of a 100 bp DNA fragment (also synthesized by Invitrogen), characteristic length of amplified PCR sequences. This choice allows demonstrating the compatibility of our technique for further application with cells population using pre-amplified DNA. In our case, this also corresponds to a larger mass at the chip surface, and thus a larger change of reflectivity induced by biological recognition.

The 100 bp DNA target sequence is the following:

 3′GCGGTCTAT**GAC**ACGATCGTCCGCATGGCGCA
 GCCATTCTCGCTGCGTTATATGCTGGTAGACGGT
 CAGGGTAACTTCGGTTCTATCGACGGCGACTC
 TG 5′.

Although our technique is label-free, we choose a labeled target in view of control experiments. Therefore, our DNA target sequence is labeled by a Cy2 molecule at 5′ end. The molecular weight of Cy2 is 714 g/mol (exCitation in blue range at $\lambda_{ex}=489$ nm and emission in green range at $\lambda_{em}=506$ nm). After specific recognition, we expect a change in the signal on probe PA (specific probe), and a lower change on probe PAmut (single nucleotide mismatch). The PE signal serves as negative control, for instance to account for non-specific binding, slight mechanical instabilities, or thermal deviation. The melting temperature (T_m) is representative

from the hybridization difference between the target and the probes. Using Integrated DNA technology (IDT) software we can determine T_m corresponding to matched (probe PA) and mismatched (probe PAmut) cases (IDT software reference). This program is based on the nearest neighbor method. It includes a correction to take into account the [Na⁺] concentration. For the match case, the T_m is 68.4 °C, whereas it drops to 58.3 °C in case of single nucleotide polymorphism, so a 10.1 °C difference. For 25 % formamide, the T_m should be corrected by 0.61 × (%formamide) so here 15 °C, decreasing melting temperatures to 53.1 °C for the match case, and 43 °C for the mismatch case. For our reaction, we therefore choose a temperature of 43 °C to see less hybridization of PAmut. The refractive index of formamide is of ~1.439 at 43 °C (Cases et al. 2001). A refractive index of 1.3595 is thus considered for peak shift analysis.

4 Results and discussion

4.1 Data acquisition and analysis

The sample is illuminated in resonant conditions, with an incidence angle of 18°. As stringent filtering conditions are applied to take benefit of near-resonance imaging, an integration time of 2 s is used to compensate for the weak incident signal.

We use 16 bits (65,536 grey levels) raw images from the Canon camera. The limit sensitivity on one pixel is $\sim 4.5 \times 10^{-4}$ (considering typical detection limited noise of 10^{-3} averaged on 5 successive images). To increase the detection limit, we can average the $\sim 50 \times 100$ pixels/micropad, reducing the noise contribution to 6×10^{-6} for each point of the profile. The images obtained are analyzed using ImageJ software and Matlab. For profiles shifts determination, we use the image correlation analysis described in Section 3.1.

4.2 Experimental process

We first place our chip with its fluidic device on the optical set-up, and introduce the 100 bp target DNA sequence specific to probe PA. DNA concentration is 50 nM in buffer consisting of 5X SSC, 0.1%m SDS, 25 % formamide. The changes in reflectivity are measured during a 45 min lapse. Stabilization is obtained after ~15 nm, when all targets are bound to the surface.

The chip is then cleaned with successive 2 min using the same solutions as for previous cleaning: (1X SSC, 0.2%m SDS), (0.1X SSC, 0.2%m SDS), and (0.1X SSC), to remove unbounded probes, prior to be observed via the fluorescence control experiment using a General Electric bioarray imager.
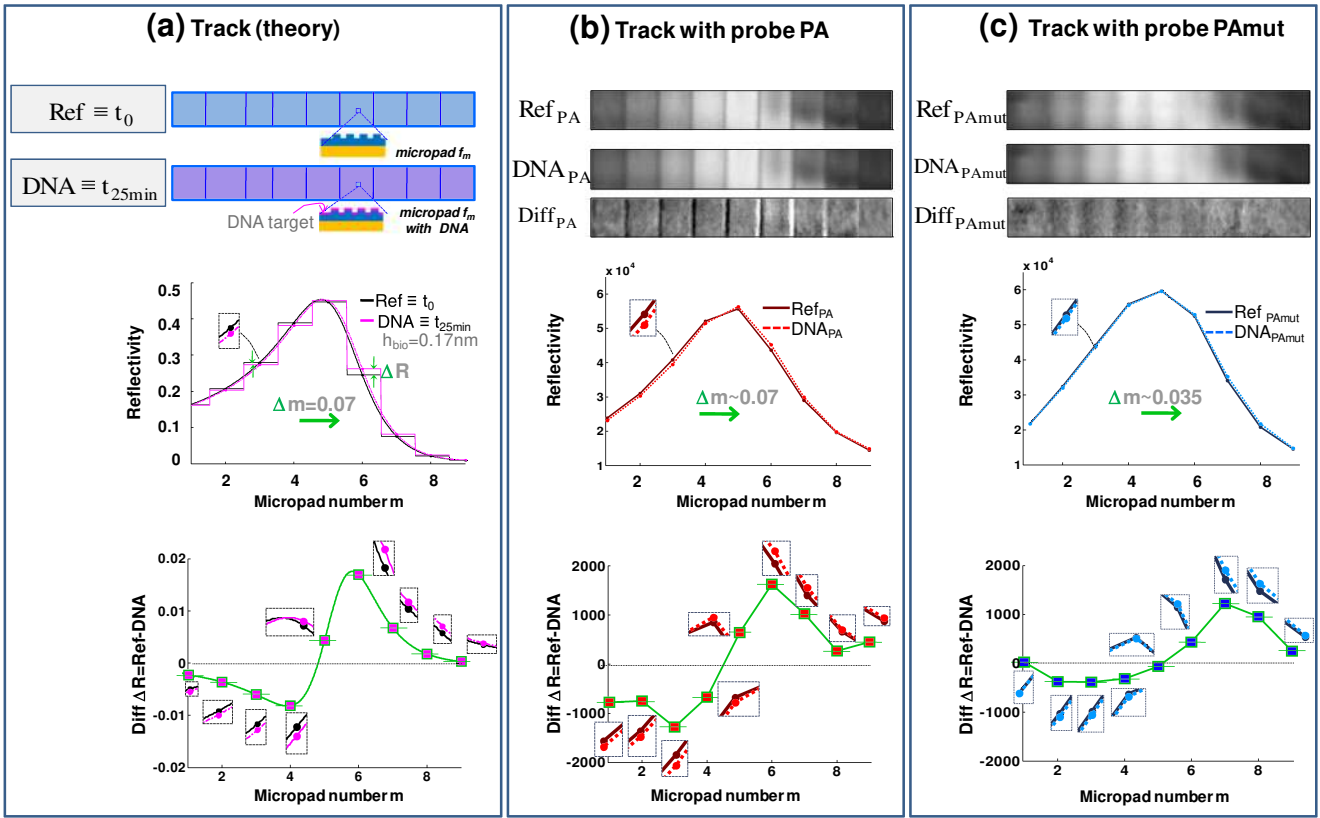
Fig. 6 **a** Scheme of the tracks and simulated reflectivity profiles R and reflectivity variation ΔR corresponding to our experimental data modeling **b** Pictures of the track PA before introduction (Ref≡t_0) and after equilibrium is reached (DNA≡$t_{25\ min}$) as well as graph with corresponding reflectivity profiles obtained by averaging pixels on each micropad and in lower part, graph with induced change in reflectivity ΔR and inset of the reflected signal values for the reference and after hybridization data (**c**) same as in (**b**) but for the track PAmut

4.3 Reflectivity variations

After probe injection, pictures of the whole chip are acquired through time, at time intervals of 12 s. We analyze the reflected signal variation through reflected images analyses. In Fig. 6, we give both simulated data corresponding to our experiment and images and profiles obtained from our experimental data.

The reference signal (Ref) on each track corresponds to $t \equiv$ t0, hence the very same track measured in hybridization buffer prior to target introduction as illustrated in Fig. 6a. As a guide to the eye, we give the simulated reflectivity data corresponding to our modeled chip (presented in Fig. 2b), but now with a 0.17 nm biological layer (~ 13 times smaller than what was illustrated in Fig. 2, chosen to illustrate what we measured in hybridization experiments detailed in what follows). A zoomed inset (magnification × 3) is also presented next to the curve, outlining in a graphically visible manner the difference in reflectivity induced by the biomolecules. The lower part of Fig. 6a gives the induced change of reflectivity ΔR, with an inset with corresponding reflectivity curves on each of the micropads. Biomolecules induce an increase of the refractive index and an apparent shift towards higher filling factor.

As a result of this shift, on micropads of filling factor less than the resonant one, the intensity decreases. Conversely, it increases on micropads with higher filling factor.

In Fig. 6b and c, we give experimental data measured on the tracks with PA and PAmut. Pictures and profiles before hybridization (Ref) and after 25 min hybridization time (DNA) are given. Reflectivity profiles are obtained by averaging $L_x \times L_y = 50 \times 30$ pixels centered on each micropad. These dimensions allow accounting for all pixels of the
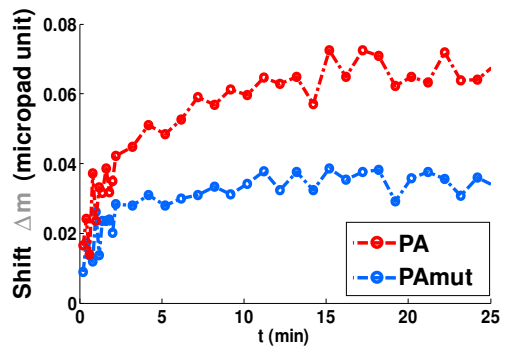

Fig. 7 Peak shift as a function of the time, after correction by the negative control contribution (temperature drift, mechanical motion...)

selected track area, as done in correlation analysis when convolving full track images, and truncating L_y dimension to correct slight chip misalignment (2°) without numerical rotation of the image.

As is seen on the figures, the PAmut track is slightly out-of-focus, since we look at an angle (Fig. 5c) and do not use a bulky telecentric lens equipment. We also checked, exactly in the spirit of distortions treated in (Bougot-Robin 2012a, b), that the chosen 50×30 pixels average takes well into account the possible larger differential signal arising at edges between micropads, whether they are in focus, as in Fig. 6b or slightly blurred as in Fig. 6c. With this simple image process, we retrieve from the experimental profiles the 'micropad width at half maximum'≈4.5 micropads, confirming our good match with the simulated data for our model of the fabricated structure. In the lower part, we also give the experimental reflectivity *variations* ΔR induced by biomolecules with insets on each of the points. Also in this case, which is more demanding, the experimental shape fits the simulated one quite well. With a signal consolidated by theoretical expectations, exploiting the whole sequence through its shift clearly allows for more robust and reliable sensing than a single point reflectivity variation ΔR_m.

In such conditions, shifts through time can now be reliably determined by the correlation analysis as introduced in Section 3.1. They are presented in Fig. 7 both for the signal measured on the sensed area PA and PAmut, corrected by the shift of the control area PE. The value at equilibrium ($t \equiv$ 25min) is indicated by an arrow on the reflectivity graphs of Fig. 6b and c. We also confirmed the end-point results using fluorescence control. To decrease noise contribution, we average 5 successive pictures (except during the 3 first minutes where there is a still a large variation of the peak position). We confirm an exponential behavior of this hybridization reaction, reaching stabilization after ~15 min. From our simulation, a shift Δm of 0.07 units corresponds to a thickness of 0.17 nm. Using the widely accepted conversion of 1 ng/mm^2 for a full surface density corresponding to 1 nm-thickness layer (Özkumur et al. 2009), such thickness is approximated to 2.2 ng/mm^2. For our molecular weight of 30.8 kDa, it corresponds to a density of 1×10^{12} molecules/cm^2. For the specific PA probe, after equilibrium is reached, the maximum shift is of $\Delta m = 0.07$ micropad. Therefore, we obtain a corresponding mass density of 171 pg/mm^2 at equilibrium. The representative noise is estimated to $\delta m = \pm 0.005$, giving a precision in mass sensitivity of 12 pg/mm^2. This sensitivity is adequate for most biology applications, and allows real-time hybridization studies. Averaging on a larger number of pictures may further increase this value. Indeed, with our present chip and set-up, only a small part of the captured picture is covered by tracks. The surface required per track is of 31×1,381 pixels in the green channel of 5,616×3,744 pixels of a raw RGB image, corresponding to 60 M pixels of 2

bytes, thus 120 MB. This means that the useful information in pixels for one monochrome track is only of 6.7×10^{-4} of the whole pixels RGB values per track. While 120 MB/image is at present an issue in data acquisition and treatment, a significant decrease by accurate coding may render averaging and computer memory less demanding. Increase of acquired pictures number by reducing the interframe time interval would allow averaging a larger number of pictures thus decreasing noise contribution to increase even further the sensitivity.

5 Conclusion

This paper demonstrates the first real-time biological study using 2D direct imaging on waveguide resonant grating. Localized gratings are used for homogeneity of probes layer, but also to scan *in situ* around the resonance by implementing tracks of micropads with varying filling factors. Through a nanopattern scanning measured on a simple picture, this offers robust measurement and a large degree of liability to validate resonant results. This is an implementation of a novel general SORCI scheme (Scan of Resonance on Chip by Imaging). The chip considered here was operating in backside detection mode, exploiting a non-reflective fluidic chamber made of black-anodized aluminum to reduce background-induced spurious fringes.

Detection of several reactions in parallel has been demonstrated using multiple tracks on a bioarray support. We focused here on real-time hybridization demonstration, using a ~30 kDa molecule. Such an experiment requires a high sensitivity, as very small variations must be detected in a time-dependent measurement. The technique currently enables sensitivities of 12 pg/mm^2 and is still mainly limited by instrumental noise.

Implementing temperature control on our fluidic chip, we could perform specific detection and detect SNP using this newly developed RWGs sensing technique. More precisely, we studied a mutation in gyrase A which has been observed in evolution studies using the *E coli* model in recently proposed microfluidic environments. SNP mutations represent the most common form of mutation (Chakravarti 2001). SNPs detection has applications in genetic disease diagnosis (Syvanen 2001), flu strain identification to distinguish pandemic and seasonal virus, cancer predisposition (Bernig et al. 2006; Lambert et al. 2011), etc.

This demonstration was realized with synthesized DNA having the typical size of a PCR fragment. Further biology studies with DNA amplified from bacteria population will be implemented. The possibility of having a self-referenced technique through imaging will make easier to deal with unspecific binding contribution, and to obtain reliable measurement from real biological sample. Thus, in principle, we will be able to quantify the fraction of a bacteria population mutated at a

given time, for instance for assessing the pathways of propagation resistance on a chip (Zhang et al. 2011a, b), or more generally for getting new insights in the understanding of cancer development (Syvanen 2001). Such analysis from bacteria could be further integrated on a single chip (Liu et al. 2008), then performing together a first PCR step (Zhang et al. 2010; Wu et al. 2009) to extract genes of interest from bacteria, and detect the portion of mutated bacteria at a given time t. This ~30 kDa molecular weight is also characteristic of proteins, thus demonstrating the generic compatibility of our technique with immune tests.

With recent progress in ultraviolet technologies (Crawford 2009) and compatibility of resonant waveguide structures with any radiation wavelength domain, an implementation for real-time hybridization experiments in ultraviolet may also be carried out, for instance exploiting data gained from UV absorption. Absorption coefficients can be calculated from DNA sequence or from amino acids sequence for proteins (Robin et al. 2009). Depending on the refractive index of reaction buffer, signals of interest might be targeted more specifically (Bougot-Robin et al. 2010).

This work demonstrates the potential of our technique toward a large range of biology application, including DNA and proteins. Knowing the growing interest of cells studies using immobilization on a chip surface for further analysis (Ferrie et al. 2010; Zhu et al. 2012), this work also opens perspectives for label-free cells studies, which is a distinctive asset of resonant waveguide gratings. Based on a simple nanopattern scanning measured with simple monochromatic imaging set-up followed by a robust image treatment step, we hope that our new technique and our so-called SORCI scheme (Scan of Resonance on Chip by Imaging) will gain large accessibility and foster numerous novel applications for real-time bioarray imaging, taking advantages of flexible RWGs characteristics.

References

A. Abbas, M.J. Linman, Q. Cheng, Anal. Chem. **83**(8), 3147–3152 (2011)

S.H. Baik, S.K. Park, C.-J. Kim, B. Cha, **39**(2), 262–267 (2007)

M. Bally, S. Syeda, A. Binkert, E. Kauffmann, M. Ehrat, J. Vörös, Anal. Biochem. **416**(2), 145–151 (2011)

T. Bernig, S.J. Chanock, Expert Rev. Mol. Diagn. **6**(3), 319–331 (2006)

K. Bougot-Robin, J.L. Reverchon, M. Fromant, L. Mugherli, P. Plateau, H. Benisty, Opt. Express **18**(11), 472–482 (2010)

K. Bougot-Robin, Shunbo Li, Y. Zhang, I.M. Hsing, H. Benisty, W. Wen, Analyst **137**(20), 4785–4794 (2012a)

K. Bougot-Robin, W. Wen, H. Benisty, Biomed. Opt. Express **3**(10), 2436 (2012b)

A.M. Cases, A.C. Gomez Marigliano, C.M. Bonatti, H.N. Solimo, J. Chem. Eng. Data **46**(3), 712–715 (2001)

A. Chakravarti, Nature **409**(6822), 822–823 (2001)

T.Y. Chang, M. Huang, A.A. Yanik, H.Y. Tsai, P. Shi, S. Aksu, M.F. Yanik, H. Altug, Lab Chip **11**(21), 3596–3602 (2011)

H. Choumane, N. Ha, C. Nelep, A. Chardon, G.O. Reymond, C. Goutel, G. Cerovic, F. Vallet, C. Weisbuch, H. Benisty, Appl. Phys. Lett. **87**(3), 031102 (2005)

M.H. Crawford, IEEE J. Sel. Top. Quant. Electron. **15**(4), 1028–1040 (2009)

A. David, Ann. Phys. (Paris) **31**(6), (2006)

A. Dhawan, M. Canva, T. Vo Dinh, Opt. Express **19**(2), 787–813, (2011)

A.M. Ferrie, Q. Wu, Y. Fang, Appl. Phys. Lett. **97**(22), 223704 (2010)

S.P. Fodor, R.P. Rava, X.C. Huang, A.C. Pease, C.P. Holmes, C.L. Adams, Nature **364**(6437), 555–556 (1993)

N. Ganesh, W. Zhang, P.C. Mathias, B.T. Cunningham, Nat. Nanotechnol. **2**(8), 515–520 (2007)

S. George, I.D. Block, S.I. Jones, P.C. Mathias, V. Chaudhery, P. Vuttipittayamongkol, H.Y. Wu, L.O. Vodkin, B.T. Cunningham, Anal. Chem. **82**(20), 8551–8557 (2010)

C. Hu, D. Liu, Mod. Appl. Sci. **4**(6), 8–13 (2010)

Integrated DNA Technologies (IDT) SciTools OligoAnalyzer 3.1 http://www.idtdna.com/analyzer/Applications/OligoAnalyzer/

C.E. Jordan, A.G. Frutos, A.J. Thiel, R.M. Corn, Anal. Chem. **69**(24), 4939–4947 (1997)

R.E. Kunz, K. Cottier, Anal. Bioanal. Chem. **384**(1), 180–190 (2006)

P.Y. Kwok, X.G. Chen, Curr. Issues Mol. Biol. **5**, 43–60 (2003)

G. Lambert, L.E. Salmeron, S. Oh, D. Liao, B.M. Emerson, T.D. Tlsty, R.H. Austin, Nat. Rev. Cancer **11**(5), 375–382 (2011)

L. Li, J. Opt. Soc. Am. A **13**(5), 1024–1035 (1996)

P. Li, B. Lin, J. Gerstenmaier, B.T. Cunningham, Sensors Actuators Chem. **99**(1), 6–13 (2004)

H. Li, H. Song, C, Rao, X. Rao, Opt. Commun. **281**(4), 750–755 (2008)

L. Liu, W. Cao, J. Wu, W. Wen, D. Choy Chang, P. Sheng, Biomicrofluidics **2**, 034103 (2008)

L. Martinelli, H. Choumane, K.N. Ha, G. Sagarzazu, C. Goutel, C. Weisbuch, T. Gacoin, H. Benisty, Appl. Phys. Lett. **91**(8), 083901 (2007)

C. Nogues, H. Leh, J. Lautru, O. Delelis, M. Buckle, PLoS One **7**(9), 44287 (2012)

R.V. Olkhov, A.M. Shaw, Anal. Biochem. **396**(1), 30–35 (2010)

R.V. Olkhov, R. Parker, A.M. Shaw, Biosen. Bioelectron. **36**(1), 1–5 (2012)

E. Özkumur, A. Yalçın, M. Cretich, C.A. Lopez, D.A. Bergstein, B.B. Goldberg, C. Marcella, M.S. Ünlü, Biosen. Bioelectron. **25**(1), 167–172 (2009)

K. Robin, J.L. Reverchon, L. Mugherli, M. Fromant, P. Plateau, H. Benisty, Biosens. Bioelectron. **24**(6), (2009)

P. Skafte-Pedersen, M. Hemmingsen, D. Sabourin, F.S. Blaga, H. Bruus, M. Dufva, Biomed. Microdevices **14**(2), 385–399 (2012)

A.C. Syvanen, Nat. Rev. Genet. **2**(12), 930–942 (2001)

K. Tawa, H. Hori, K. Kintaka, K.Kiyosue, Y. Tatsu, J. Nishii, Opt. Express **16**(13), 9781–9790 (2008)

S. Tonchev, O. Parriaux, Photon. Nanostruct. Fundam. Appl. **10**(4), 651–656 (2012)

J. Wu, W. Cao, W. Wen, D. Choy Chang, P. Sheng, Biomicrofluidics **3**, 012005 (2009)

J. Wu, G. Zheng, L.M. Lee, Lab Chip **12**(19), 3566–3575 (2012)

Q. Xiang, B. Xu, D. Li, Biomed Microdevices, **9**(4), 443–449 (2007)

E.M. Yeatman, Biosens. Bioelectron. **11**, 635–649 (1996)

Y. Zhang, S. Park, S. Yang, T.H. Wang, Biomed. Microdevices **12**(6), 1043–1049 (2010)

Q. Zhang, G. Lambert, D. Liao, H. Kim, K. Bougot-Robin, C.K. Tung, N. Pourmand, R.H. Austin, Science **333**(6050), 1764–1767 (2011a)

Q. Zhang, K. Bougot-Robin, D. Liao, G. Lambert, R.H. Austin, Mol. Pharm. **8**(6), 2063–2068 (2011b)

J. Zhu, T. Nguyen, R. Pei, M. Stojanovic, Q. Lin, Lab Chip **12**, 3504–3513 (2012)